Discrete-phase effects on the flow field of a droplet-laden swirling jet with recirculation: A numerical study

J. S. Anagnostopoulos and G. C. Bergeles
Fluids Section, Department of Mechanical Engineering, National Technical University of Athens, Athens, Greece

A numerical algorithm based on the Lagrangian approach for the discrete phase and on the Eulerian for the continuous phase has been developed and used to predict a two-phase, droplet-laden swirling jet flow in a quarl geometry. The gas-phase equations are discretized using finite difference principles and are solved with the aid of the SIMPLE algorithm. The dispersion of the discrete phase is simulated using a stochastic separated flow model. After the reliability tests, the method is used to quantify the effects of droplet size, droplet loading, and swirl intensity on the carrier phase internal recirculation region and on the dispersion of droplets. The results indicate that the amount of recirculating mass increases with the droplet diameter and the decrease of loading. For high loadings and swirl the internal recirculation region breaks down and it is divided into two subregions. Small droplets are dispersed following the gas phase, while large droplets are affected mainly by their injection conditions.

Keywords: droplet-laden; swirl; jet; recirculation; numerical

Introduction

The particle-laden, swirling, turbulent jet is a type of flow common in solid and liquid fueled burners. The swirl, combined with the divergent nozzle (quarl), creates an internal recirculation zone (IRZ) near the axis and in the vicinity of the burner, which accelerates the rate of mixing and improves combustion efficiency.

Several investigations, experimental and numerical, are available in the literature, concerning particle-laden, axisymmetric flows. In general, the presence of the particle phase in a free jet of air causes reduction of the rate of the axial fluid velocity decay and of the jet radial spread, because of the momentum exchange between the two phases.[1] This momentum exchange was found by Tsuji *et al.*[2] to be higher for smaller particles. The dispersion of small particles is caused by their interaction with the continuous phase turbulence,[3] while the injection conditions play an important role in the dispersion of big particles, as found by Hayashi and Branch.[4] The latter researchers also found that the use of divergent nozzles increases the dispersion of the particle phase.[5]

However, all the above investigations are for flows without swirl and recirculation. Certain other investigations address the issue of swirling flows with recirculation in divergent nozzles, but these works deal with one-phase gas flows (i.e., Dixon *et al.*[6]). The measurements of Liu *et al.*[7] and Hardalupas *et al.*[8] constitute the only available information on particle-laden swirling jet flows with recirculation when a quarl is present at the jet exit. However, the measurements of the first researchers refer to a dense, solid–liquid flow, where the by volume content of the discrete phase is significant. On the contrary, the work of Hardalupas *et al.*[8] refers to a dilute, two-phase flow of kerosene with air, under conditions analogous to those met in combustion systems. In addition, this work contains detailed information about the inlet conditions of both phases.

There are two theoretical approaches in studying the two-phase flow problems: the Eulerian approach, which assumes the particulate phase to be a continuum (i.e., Elgobashi and Abou-Arab[9]) and the Lagrangian approach, which treats the particulate phase in a discrete manner (i.e., Migdal and Agosta[10]). Comparisons of the two approaches along with enumeration of each one's merits are available elsewhere.[11,12] The method used in this study is based on the Lagrangian approach, which is more suitable for the examined types of flow (i.e., low volume fraction, variable droplet diameter, etc.).

The reliability of the present code in predicting particle-laden flows has been established in the works of Anagnostopoulos and Bergeles[13] and Sargianos *et al.*[14]

The purpose of the present work is to establish the effect of various parameters, defining the discrete phase, on the topology of the recirculation zone in a quarl geometry found in many engineering applications.

Briefly, the work to follow includes (1) validation of the reliability of the numerical code for complex, two-phase flows by comparing predictions to the experimental data of Hardalupas *et al.*[8]; (2) parametric study of the effects of droplet size and droplet loading on the IRZ; and (3) study of the influence of droplet size, droplet loading, and swirl intensity on droplets' dispersion.

Theoretical analysis

Equations for the continuous gas phase

The governing equations for the incompressible gas phase in cylindrical, axisymmetric coordinates and for steady state

Address reprint requests to Dr. Bergeles at the Department of Mechanical Engineering, National Technical University of Athens, Athens, Greece.

Received 3 October 1990; accepted 14 November 1991

conditions are

Continuity:

$$\frac{\partial U}{\partial x}+\frac{1}{r}\frac{\partial}{\partial r}(rV)=0 \tag{1}$$

Axial momentum:

$$\frac{\partial}{\partial x}(\rho UU)+\frac{1}{r}\frac{\partial}{\partial r}(\rho rVU)=-\frac{\partial p}{\partial x}+\frac{\partial}{\partial x}\left(\mu_{eff}\cdot\frac{\partial U}{\partial x}\right)+\frac{1}{r}\cdot\frac{\partial}{\partial r}\left(r\cdot\mu_{eff}\cdot\frac{\partial U}{\partial r}\right)+\frac{\partial}{\partial x}\left(\mu_{eff}\cdot\frac{\partial U}{\partial x}\right)+\frac{1}{r}\cdot\frac{\partial}{\partial r}\left(r\cdot\mu_{eff}\cdot\frac{\partial V}{\partial x}\right) \tag{2}$$

Radial momentum:

$$\frac{\partial}{\partial x}(\rho UV)+\frac{1}{r}\frac{\partial}{\partial r}(\rho rVV)=-\frac{\partial p}{\partial r}+\frac{\partial}{\partial x}\left(\mu_{eff}\cdot\frac{\partial V}{\partial x}\right)+\frac{1}{r}\cdot\frac{\partial}{\partial r}\left(r\cdot\mu_{eff}\cdot\frac{\partial V}{\partial r}\right)+\frac{\rho\cdot W^2}{2}-2\mu_{eff}\cdot\frac{V}{r^2}+\frac{\partial}{\partial x}\left(\mu_{eff}\cdot\frac{\partial U}{\partial r}\right)+\frac{1}{r}\cdot\frac{\partial}{\partial r}\left(r\cdot\mu_{eff}\cdot\frac{\partial V}{\partial r}\right) \tag{3}$$

Circumferential momentum:

$$\frac{\partial}{\partial x}(\rho UW)+\frac{1}{r}\frac{\partial}{\partial r}(\rho rVW)=\frac{\partial}{\partial x}\left(\mu_{eff}\cdot\frac{\partial W}{\partial x}\right)+\frac{1}{r}\cdot\frac{\partial}{\partial r}\left(r\cdot\mu_{eff}\cdot\frac{\partial W}{\partial r}\right)-W\cdot\left(\frac{\rho\cdot V}{r}+\frac{\mu_{eff}}{r^2}+\frac{1}{r}\cdot\frac{\partial\mu_{eff}}{\partial r}\right) \tag{4}$$

where U, V, and W are the axial, radial, and circumferential mean gas velocities in the respective x, r, and ∂ directions.

Introducing the turbulent exchange coefficient:

$$\Gamma_\varphi=\mu_{eff}/\sigma_\varphi \tag{5}$$

where σ_φ is the appropriate Schmidt/Prandtl number for the Φ transportable quantity; all the above equations can be cast into the common form:

$$\rho\cdot\frac{\partial}{\partial x}(U\Phi)+\rho\cdot\frac{1}{r}\cdot\frac{\partial}{\partial r}(rV\Phi)=\frac{\partial}{\partial x}\left(\Gamma_\varphi\cdot\frac{\partial\Phi}{\partial x}\right)+\frac{1}{r}\cdot\frac{\partial}{\partial r}\left(r\Gamma_\varphi\cdot\frac{\partial\Phi}{\partial r}\right)+S_\varphi+S_{d,\varphi} \tag{6}$$

where S_φ is a source term and $S_{d,\varphi}$ is an additional source to account for the momentum exchange between the continuous and discrete phases.

The above equation for $\Phi=1$ results into the continuity equation, and for $\Phi=U$, V, W produces the momentum equations. Also, for $\Phi=\mathrm{k}$ and $\Phi=\varepsilon$ gives appropriate expressions for the turbulent kinetic energy (k) and its rate of dissipation (ε) of the two-equation k-ε turbulence model,[15] which is used in the present study as a turbulence closure. The effective turbulent viscosity is calculated via the relation

$$\mu_{eff}=\mu+\mathrm{C}_\mu\cdot\rho\cdot\mathrm{k}^2/\varepsilon \tag{7}$$

where μ is the laminar viscosity of the air and C_μ is a constant of the turbulence model.

Expressions for the turbulent diffusivity Γ_φ and the source terms S_φ are given in Table 1, whereas the form of the source terms $S_{d,\varphi}$ due to the presence of droplets is written in the next paragraph.

Equations for the discrete phase

The stochastic model used for the simulation of the liquid-phase dispersion includes the calculation of trajectories of a representative number of droplets, using for their instantaneous motion, Lagrangian equations of the form

$$du_d/dt=A\cdot(u-u_d)+g \tag{8}$$

Notation

C_μ, C_1, C_2	Coefficients in the turbulence model
C_D	Drag coefficient
D	Nozzle diameter
D_d	Droplet diameter
g	Gravitational acceleration
k	Turbulent kinetic energy
L_e	Eddy size
Lr	Length of IRZ
m_d	Droplet mass flow rate
Mr	Recirculating mass
P	Static pressure
r	Distance in the radial direction
Re	Reynolds number
S_φ, $S_{d,\varphi}$	Source terms due to gas and droplet phase
S_n	Swirl number
t	Time
T_e	Eddy lifetime
U, u	Mean and instantaneous axial velocity
V, v	Mean and instantaneous radial velocity
W, w	Mean and instantaneous circumferential velocity
x	Distance in the axial direction

Greek symbols

Γ_φ	Turbulent exchange coefficient
ε	Kinetic energy dissipation rate
μ	Laminar viscosity
μ_{eff}	Effective viscosity
ρ	Material density
σ_φ	Schmidt/Prandtl number

Subscripts

0	Conditions at the nozzle exit
d, p	Dispersed phase

Abbreviations

IRZ	Internal recirculation zone
SMD	Sauter mean diameter

Table 1 Turbulent diffusivity and source terms of Equation 6

Φ	Γ_φ	S_φ
1	0	0
U	μ_{eff}	$-\frac{\partial P}{\partial x}+\frac{\partial}{\partial x}\left(\mu_{eff}\cdot\frac{\partial U}{\partial x}\right)+\frac{1}{r}\cdot\frac{\partial}{\partial r}\left(r\cdot\mu_{eff}\cdot\frac{\partial V}{\partial x}\right)$
V	μ_{eff}	$-\frac{\partial P}{\partial r}+\frac{\partial}{\partial x}\left(\mu_{eff}\cdot\frac{\partial U}{\partial r}\right)+\frac{1}{r}\cdot\frac{\partial}{\partial r}\left(r\cdot\mu_{eff}\cdot\frac{\partial V}{\partial r}\right)+\frac{\rho\cdot W^2}{2}-2\mu_{eff}\cdot\frac{V}{r^2}$
W	μ_{eff}	$-W\cdot\left(\frac{\rho\cdot V}{r}+\frac{\mu_{eff}}{r^2}+\frac{1}{r}\cdot\frac{\partial\mu_{eff}}{\partial r}\right)$
k	$\frac{\mu_{eff}}{\sigma_k}$	$G-\rho\cdot\varepsilon$
ε	$\frac{\mu_{eff}}{\sigma_\varepsilon}$	$\varepsilon/\mathrm{k}\cdot(\mathrm{C}_1\cdot G-\mathrm{C}_2\cdot\rho\cdot\varepsilon)$
G	$=\mu_{eff}\left[2\cdot\left\{\left(\frac{\partial U}{\partial x}\right)^2+\left(\frac{\partial V}{\partial r}\right)^2+\left(\frac{V}{r}\right)^2\right\}+\left(\frac{\partial W}{\partial x}\right)^2+\left(\frac{\partial U}{\partial r}+\frac{\partial V}{\partial x}\right)^2+\left(\frac{\partial W}{\partial r}-\frac{W}{r}\right)^2\right]$	
$C_\mu=0.09$,	$C_1=1.44$,	$C_2=1.92$, $\sigma_k=0.9$, $\sigma_\varepsilon=1.3$

$$dv_d/dt = A\cdot(v-v_d)+w_d^2/r \tag{9}$$

$$dw_d/dt = A\cdot(w-w_d)-v_dw_d/r \tag{10}$$

and

$$d\vec{s}_d/dt = \vec{u}_d \tag{11}$$

where

$$A=\frac{3}{4}\frac{\mu}{\rho_dD_d^2}\cdot C_D\cdot\mathrm{Re}_d \tag{12}$$

where u and u_d are the instantaneous fluid and droplet velocities, respectively, ρ_d the droplet density, and D_d the droplet diameter. The drag coefficient C_D is taken from Wallis[16] as

$$C_D=(1+0.15\cdot\mathrm{Re}_d^{0.687})/(\mathrm{Re}_d/24) \quad \text{for } \mathrm{Re}_d\leqslant 1{,}000 \tag{13}$$

$$C_D=0.44 \quad \text{for } \mathrm{Re}_d>1{,}000 \tag{14}$$

where the droplet Reynolds number is

$$\mathrm{Re}_d=\rho\cdot|\vec{u}-\vec{u}_d|\cdot D_d/\mu \tag{15}$$

The flow field is assumed to be composed of eddies with characteristic length and lifetime[17]:

$$L_e=\mathrm{C}_\mu^{3/4}\mathrm{k}^{3/2}/\varepsilon \tag{16}$$

$$T_e=L_e/(2\mathrm{k}/3)^{1/2} \tag{17}$$

Each droplet interacts with an eddy until it gets out of it or until the eddy lifetime is exceeded. The instantaneous gas velocities appearing in Equations 8–11 are taken to be constant as long as the interaction lasts; they are computed using the mean values of the flow field and the following relation:

$$\varphi=\Phi+\varphi', \quad \varphi=u,\ v, \text{ and } w \tag{18}$$

where the fluctuation φ' follows Gaussian distribution with standard deviation[17]:

$$\sigma=(2\mathrm{k}/3)^{1/2} \tag{19}$$

During the motion of droplets, the change in their momentum results in equivalent changes of the gas-phase momentum, which are expressed via source terms of the form

$$S_{d,\varphi}=m_d\cdot[(u_{d,in}-u_{d,out})+g\cdot(1-\rho/\rho_d)\cdot(t_{in}-t_{out})] \tag{20}$$

where m_d is the mass flow rate of a droplet and t is the time; the quantities with subscripts *in* and *out* refer to the time instants that a droplet enters or leaves a computational control volume (Figure 1).

Solution method

Discretization

The computational domain has been divided in control volumes, with the aid of a nonuniform 35 × 40 orthogonal grid (Figure 2). A staggered grid arrangement has been used in which the scalar quantities are stored at the grid nodes, while the velocities are placed equidistantly between the nodes.

A hybrid difference scheme, which combines upwind and central differencing techniques, depending on the local Peclet number, has been used for the discretization of the gas-phase equations. After discretization, the form of the equation obtained is

$$A_p\cdot\Phi_p=\sum_i(A_i\cdot\Phi_i)+S_\varphi+S_{d,\varphi}, \quad i=\text{east, west, north, south} \tag{21}$$

The finite difference equations are solved iteratively, using the SIMPLE algorithm of Patankar and Spalding.[18]

The following technique has been used for the quicker and more accurate integration of the equations of droplet motion. For a very small time step of integration it is assumed that the droplet Reynolds number is constant. This way, Equations 8–11, transformed in Cartesian coordinates, can be solved analytically. This technique is fast in solving the equations, because it does not make use of any integration methods and also ensures accuracy of results near the axis, where other conventional iteration methods need special treatment to converge to correct results.[19]

To estimate the source terms $S_{d,\varphi}$ of Equation 6, knowledge

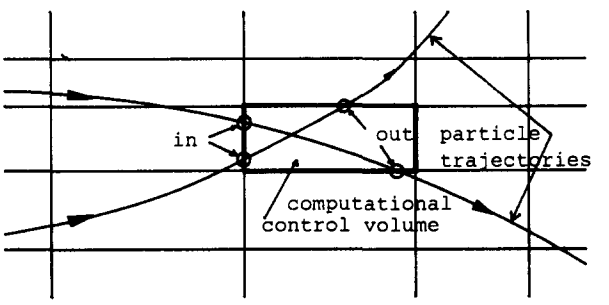

Figure 1 Calculation of particle source terms

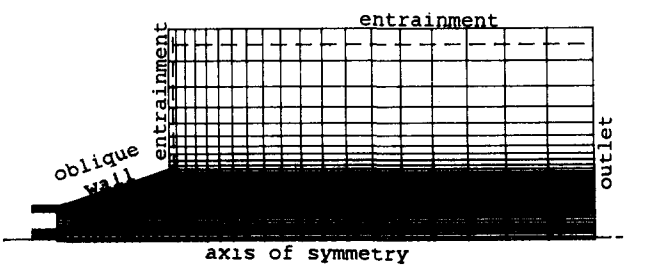

Figure 2 Computational grid (35 × 40 nodes)

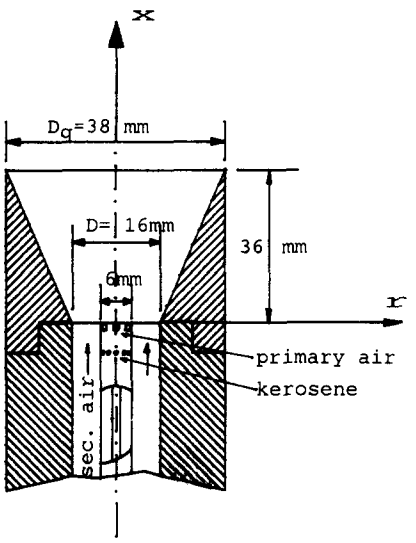

Figure 3 Test case of Hardalupas *et al.*[8] (isothermal, kerosene-air flow)

of the discrete-phase momentum is required at two time instants: (1) when the droplets enter a computational cell and (2) when they leave it. A fast "predictor-corrector" scheme, described in detail in the work of Diakoumakos *et al.*,[20] has been adopted for the calculation of the values needed.

The same technique has been used to estimate the time of integration between droplets and eddies. This technique has the advantage that it is capable of calculating the droplet motion, considering variable droplet acceleration.

The test geometry

The experimental setup of Hardalupas *et al.*,[8] as it is shown in Figure 3, consists of a vertical, axisymmetric burner with quarl. The quarl length is two burner diameters and the quarl angle is 20°. The Reynolds number is 30,000. Primary air is injected through six 1.0-mm holes, and liquid kerosene is added through a second set of six 0.33-mm holes in the circumference of the central tube (Figure 3). Hardalupas *et al.*[8] measured the mean and fluctuating quantities of both phases at the outlet of the burner pipe, without the quarl. Measurements have also been reported for the droplet concentration profiles and diameter distribution for three different diameter classes: $5 \div 10\ \mu m$, $25 \div 30\ \mu m$, and $55 \div 60\ \mu m$, having Stokes numbers of 33.6, 3.7, and 0.97, respectively. The axial field symmetry is affected by the presence of the holes, and for this reason, measurements in three different radial directions are given.

The numerical solution has made use as inlet condition the mean of the values in these three locations. Also, as has been observed by Hardalupas *et al.*,[8] the presence of the quarl has only a little effect on the inlet values found experimentally; therefore, the measurements taken without quarl have been used for calculations. Table 2 summarizes the experimental conditions at the inlet.

Boundary conditions

A stair-step approximation has been used to simulate the divergent quarl (Figure 4). "Wall functions" for the velocity components and turbulent quantities (k and ε) have been used for the internal nodes, which are adjacent to the solid boundaries.

Entrainment conditions have been used for the left and top boundaries (Figure 2), to simulate the correct mass of ambient air induced inward.

The experimental data of Hardalupas *et al.*[8] are used at the inlet of the computational domain, which starts from the beginning of the quarl. The outlet velocity results from a mass balance and parabolic type of flow boundary conditions.

Solid body rotation assumption has been made for the tangential velocity at the centerline, whereas for the other quantities the condition is $\partial\Phi/\partial r = 0$, except for velocity, for which $V = 0$ is used.

The calculation of a droplet trajectory stops when the droplet gets out of the computational domain. If a droplet strikes the oblique wall, the strike is assumed to be perfectly elastic.

Assumptions and limitations

Although it has been reported[21] that the k-ε turbulence model exhibits deficiencies in swirling flows, concerning both mean and fluctuating flow predictions, it was found that in our case the standard k-ε model works in a more consistent manner than various modifications that have been suggested in the literature (i.e., Leschziner and Rodi[22]) and tested in the present work.

Turbulence is assumed to be isotropic: at any point, the standard deviation of the velocity fluctuations is the same in all three directions (Equation 19).

The droplets are assumed to be spherical, an assumption very close to reality.

The assumption of perfectly elastic droplet strike is not so realistic for liquid droplets, but the predictions of the experimental case examined showed that the percentage of droplets arriving at the oblique wall is small.

The droplet volume fraction of the examined cases is almost

Table 2 Inlet conditions of Hardalupas *et al.*[8]

Reynolds number	30,000
Swirl number	$S_n = 0.5$
$S_n = \dfrac{\int_{R_1}^{R_2} \rho \cdot U \cdot W \cdot dr}{R_2 \int_{R_1}^{R_2} \rho \cdot U^2 \cdot dr}$	
Mass loading	14 percent
Droplet density	780 kg/m³
Droplet SMD	62 μm
$\text{SMD} = \dfrac{\int D_d \cdot n(D_d) \cdot dD_d}{\int D_d^2 \cdot n(D_d) \cdot dD_d}$	

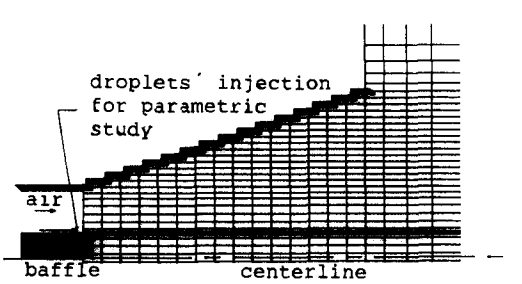

Figure 4 Detail of computational grid inside the quarl; stair-step approximation of the oblique wall

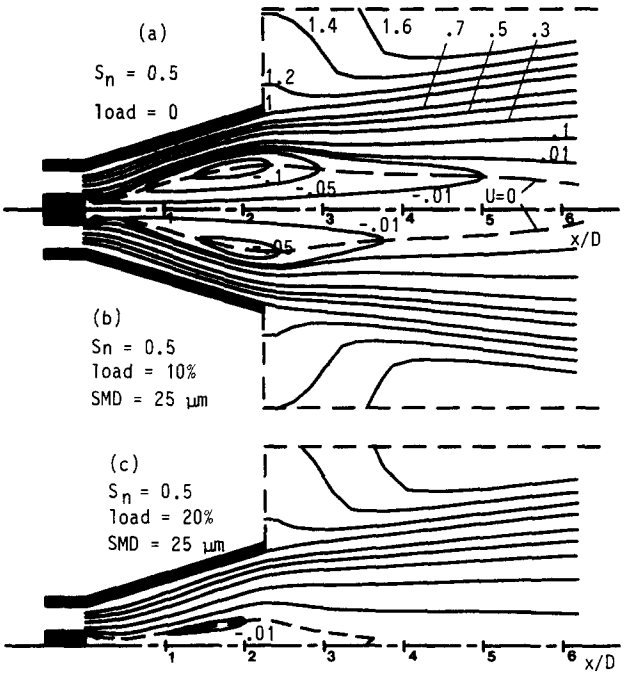

Figure 5 Contours of stream function for $S_n = 0.5$ and droplet SMD = 25 μm

zero, and thus it has not been taken into account in the gas-phase equations. Collision, aggregation, and interaction of any kind among droplets has been neglected for the same reason. Several other forces acting on the droplets are also unimportant according to the literature, i.e., Basset forces because $\rho_p/\rho \gg 1$ and Magnus forces because $d_p \ll 1$ mm.

The droplets have been divided in groups. All droplets of the same group have the same injection conditions, and they follow identical trajectories. The diameter distribution has been divided in 10 ranges, 10 μm each in width (between 0 and 100 μm[8]). Up to 1,000 groups are found to be sufficient for an adequate statistical representation of the discrete phase for all cases. For the final results of the discrete phase and in order to eliminate scattering, a number of groups one order of magnitude higher has been considered. The trajectories of these groups have been computed only once and after the total flow field had been computed.

Solution procedure: convergence

The gas-phase equations are iteratively solved until convergence is achieved, without the presence of droplets. Then, the droplets are injected into the converged flow field and during the calculation of their trajectories, the source terms, representing the momentum exchange between the two phases, are computed and stored.

The equations of the gas phase are solved again, using the new source terms, producing a different flow field. This process is repeated until the quantities of both phases converge. Criterion for convergence is that between two consecutive iterations, the droplets source terms and the gas-phase quantities remain almost unchanged.

The number of iterations between gas flow field and discrete phase varies from 4 to about 10, depending on the droplet loading.

Additional information

The computer runs required for this study have been performed on an AT, IBM compatible personal computer (10 MHz) with coprocessor, under a DOS operating system. A 35 × 40 nonuniform grid has been used, with about 250 grid nodes being within the quarl. The storage requirements for such a grid are about 300 Kb and the time needed for each iteration of the gas-phase code is about 30 seconds. The time needed for the calculation of each group of droplets' trajectory is about 5 seconds.

The underrelaxation factor used is 0.6 for the velocities and turbulence quantities, 0.4 for the pressure, and from 0.2–1 for the droplet source terms (depending on the mass loading).

The total time required for the converged solution may be reduced considerably with the use of an optimum combination of underrelaxation factors for the droplet source terms.

The results obtained with the 35 × 40 mesh agreed within 5 percent with the results obtained using a finer grid of 50 × 60 nodes.

Presentation and discussion of results

Test of the reliability of the numerical method

In Figure 5a, the predicted flow field of the experimental arrangement of Hardalupas *et al.*[8] is shown. In this figure one can distinguish the IRZ, which is created due to the existence of swirl and the divergent nozzle too. The mass carried away, as it has been calculated with the aid of entrainment conditions, can also be seen in the same figure.

In Figures 6 and 7 there are comparisons of predictions with experimental data. These figures include axial velocities of small (7.5 μm diameter) and big (57.5 μm diameter) kerosene droplets at various downstream positions.

The small droplets practically follow the fluid streamlines, like massless fluid particles, reversing the direction of their

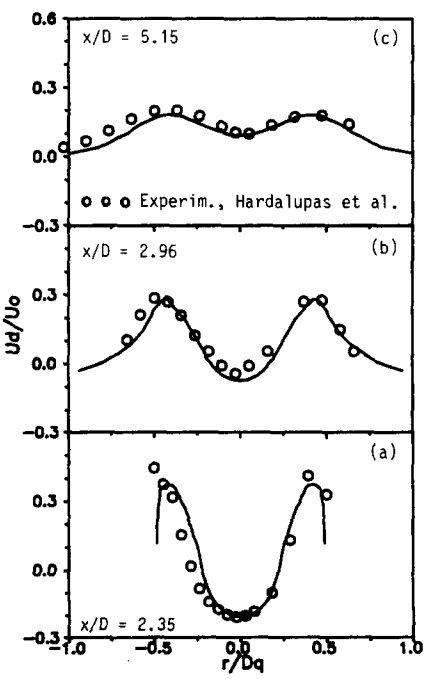

Figure 6 Axial droplet velocity profiles: ———, predictions for $D_d = 7.5$ μm; Uo = gas inlet bulk velocity

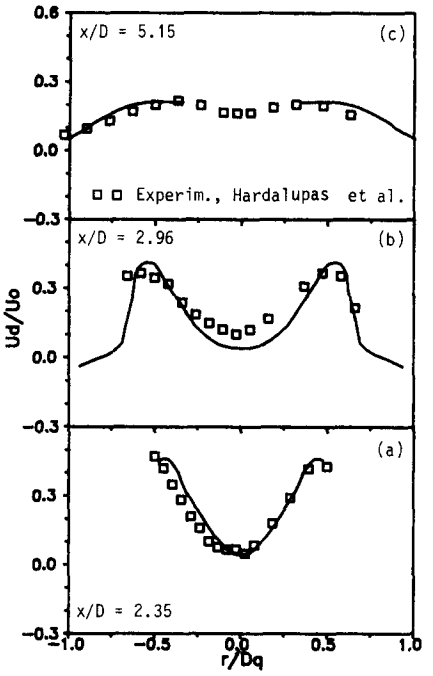

Figure 7 Axial droplet velocity profiles: ———, predictions for $D_d = 57.5$ μm; Uo = gas inlet bulk velocity

motion within the IRZ (Figure 6a and b). On the contrary, the big droplets, due to their high inertia, traverse the IRZ like bullets, without obtaining negative velocities (Figure 7). The above are also evident in Figure 8, where some mean trajectories of the two droplet categories are plotted.

The differences in motion and dispersion of small and big droplets indicate that, under combustion conditions, the evaporation and combustion processes will occur in different positions of the flow field, depending on the droplet diameter.

Predictions of the numerical code are in satisfactory agreement with the experimental data for both droplet categories (Figures 6 and 7). Some observable differences in the region of high velocities of big droplets (Figure 7) are probably due to uncertainties in their injection velocity (see The test geometry), which is the main factor controlling their motion. None of the 10,000 big droplets is found to pass near the axis, at a downstream distance of 4.9 pipe diameters (Figure 7c). This has also been observed experimentally, because a very large measuring time has been needed for the collection of a satisfactory sample in this region.[8]

The conclusion is that the numerical model is capable of predicting correctly the aerodynamic field of the flow and on the other hand, according to our previous experience[13,14] and the present detailed study, the stochastic model for the dispersion of droplets is reliable in complex cases too.

Parametric study

The characteristics of the IRZ are always of importance to engineers, because it is within this zone that, during combustion, intense mixing of fuel with air occurs.

The same geometry has been used for the present parametric study, with inlet conditions like those of the gas phase. For the inlet conditions of the discrete phase, it has been assumed that all droplets are injected axially from the same injection point (Figure 4). This assumption has been made in order to avoid the dependence of results on the inlet droplet concentration and velocity profiles. The distribution of droplet diameters remained the same as previously.

The flow field has been solved for two different swirl numbers (0.5 and 1.0) for a series of mass loadings from 10–90 percent and for two different droplet Sauter mean diameters (SMD), viz 25 and 62 μm. In total, 20 different computer runs have been performed.

Effect of liquid phase on recirculating mass. The swirl number S_n is defined as the ratio of tangential over axial fluid momentum. The discrete phase, which is injected axially, adds axial momentum to the continuous phase, while at the same time, it damps the circumferential momentum of the fluid. So, S_n is reduced downstream, depending on the extent of interaction between the two phases. This reduced S_n is termed "effective" S_n. The higher the momentum exchange between the two phases, the lower the effective S_n of a two-phase jet becomes. This implies that the effective S_n decreases with decreasing droplet inertia and increasing droplet loading.

Small droplets ($SMD = 25$ μm). The recirculating mass in the IRZ seems to be reduced as the loading increases (Figures 5a and b and 9a and b). It was found that for high loadings the IRZ is reduced to a small region just behind the buffer (Figure 5c); however, when the swirl number is high, the elimination of the IRZ becomes more difficult. In this case it is observed that the zone is divided into two regions, between which penetration appears (Figures 9c and d). As the loading increases, the off-axis region tends to disappear, while the zone behind the baffle persists.

Big droplets ($SMD = 62$ μm). Analogous effects have been found when the bigger droplets have been used. However, as it is shown in Figures 10 and 11, the appearance of these effects is shifted for higher loadings. The bigger droplets, due to their greater inertia, are affected more slightly by the gas phase, and the momentum exchange between the two phases is delimited. Hence, the effective S_n is higher for the big droplets compared with that of small droplets for the same loading.

Quantitative view. The above mentioned results are plotted quantitatively in Figure 12. The rate of change of the recirculating mass is higher as the swirl becomes lower and the mean droplet diameter is reduced.

In Figure 12, an almost linear decrease of the recirculating mass with increasing droplet loading, for both swirl numbers and droplet magnitudes, is apparent up to the point that the off-axis IRZ disappears. At this point, the inclination of the curves of Figure 12 is reduced drastically, as the small IRZ that stays behind the buffer is preserved. It is also worth mentioning that the difference in the rate of decrease of the recirculating mass, between the big and the small droplets, is almost independent of the swirl intensity.

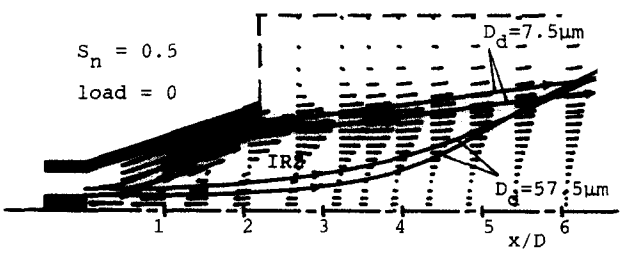

Figure 8 Indicative droplet mean trajectories for the experimental case of Hardalupas *et al.*[8]

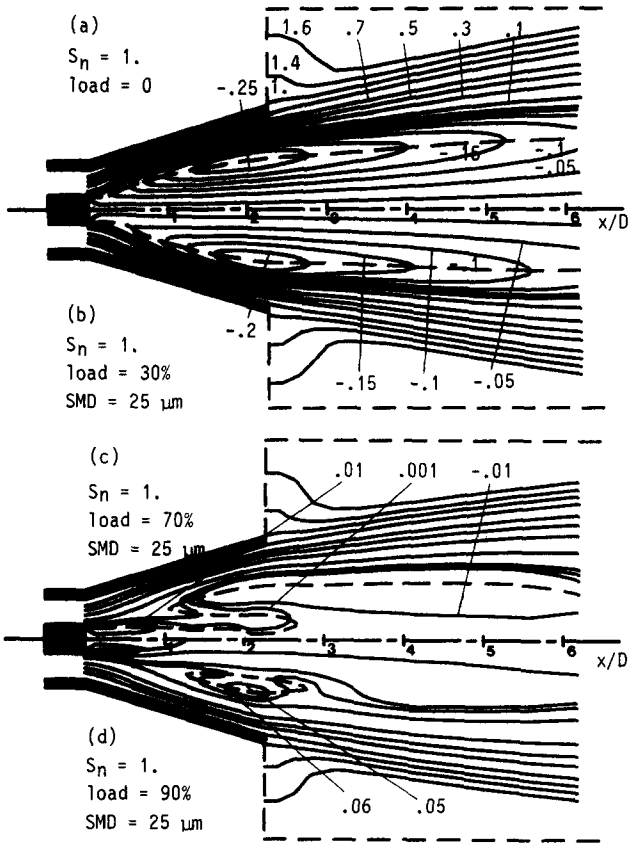

Figure 9 Contours of stream function for $S_n = 1$ and droplet SMD = 25 μm

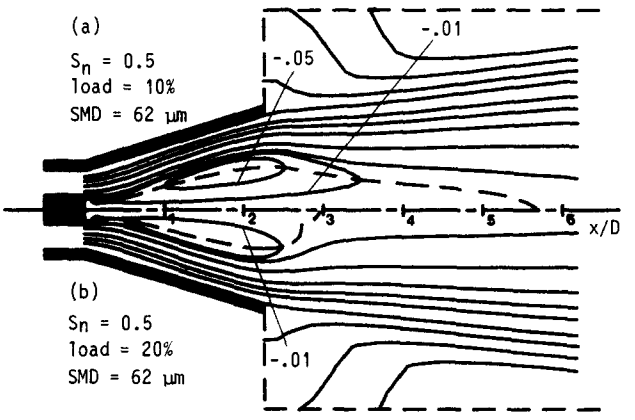

Figure 10 Contours of stream function for $S_n = 0.5$ and droplet SMD = 62 μm

Another observation from the present series of results is that the center of the main recirculation zone (at least as long as it exists) remains almost in the same position for a given swirl number of the gas phase, although the effective swirl number of the system of both phases is altered with the loading (Figures 5, 9–11). It is concluded that the geometric characteristics of the burner and the air velocity profiles at the inlet are the major factors that determine the position of this center.

Effect of discrete phase on the length of the IRZ. The length of the recirculation zone is defined as the distance between the upstream and the downstream stagnation point ($U = 0$) on the axis of symmetry of the flow. Due to the existence of the buffer, the upstream stagnation point is always found behind it, at $x = 0$.

The length of the IRZ, as a function of loading and inlet S_n is plotted in Figure 13 for the two categories of droplet

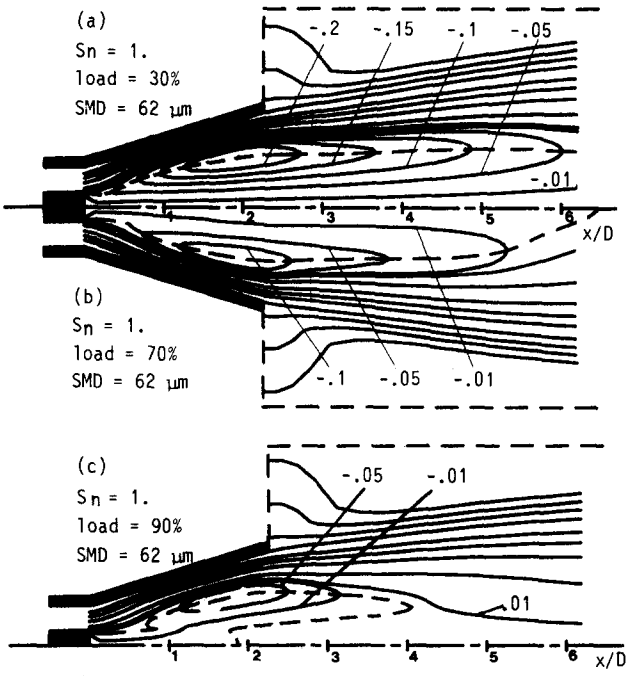

Figure 11 Contours of stream function for $S_n = 1$ and droplet SMD = 62 μm

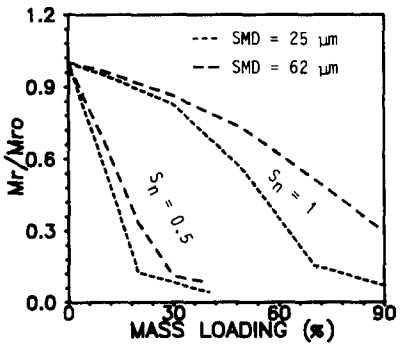

Figure 12 Variation of recirculating mass (Mr) due to the droplet loading

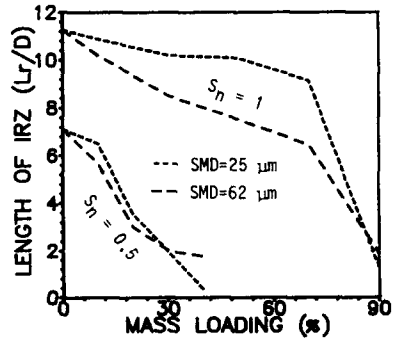

Figure 13 Variation of the length (Lr) of the IRZ due to the droplet loading

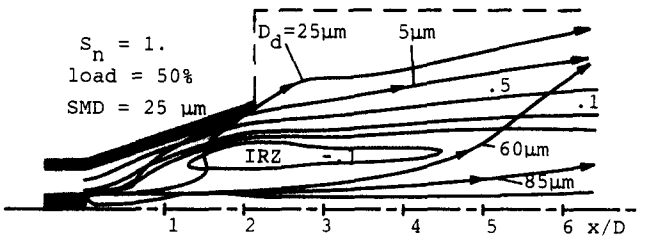

Figure 14 Indicative mean trajectories of small and big droplets for the parametric study test case

diameters examined. The length of the IRZ decreases almost linearly with the loading in the case of low swirl ($S_n = 0.5$). In this case, the magnitude of the IRZ seems to be marginally bigger for the small droplets and for a wide range of loadings ($0 \div 20$ percent), although the recirculating mass is less (Figure 12a). The same observation is more pronounced for the case of strong swirl ($S_n = 1$, Figure 13).

These results may be explained with the help of Figure 14, where mean trajectories of small and big droplets are plotted, along with fluid streamlines, for 50 percent loading and $S_n = 1$. In this figure it is observed that the big droplets traverse the IRZ and consequently they interact with it all along its length, affecting all its characteristics (recirculating mass, magnitude). On the contrary, the interaction of small droplets with the IRZ is complex: these droplets quickly exchange their initial momentum with the fluid and they are centrifuged out of the IRZ early. After that they are accelerated again along the direction of the main flow, because they are now in the region of high air velocities. Near the end of the IRZ, the axial velocity of the air phase is decreased faster than the droplet velocity, so the small droplets again give axial momentum to the fluid in the off-axis region.

As the droplet loading is augmented, the increase in the droplet momentum finally causes the IRZ to break (Figures 9c and d). At this stage, the small droplets commence to penetrate the IRZ too. So the previous mechanism ceases to exist and the length of the IRZ is reduced steeply.

Droplet distribution

In order to study the distribution of the discrete phase, the SMD = 25 μm droplets have been divided into two categories of equal mass each. One of them includes the small droplets, with SMD = 15 μm, and the other the big droplets, with SMD = 100 μm.

Big droplets. Due to their high inertia, the injection conditions of the big droplets (mean and fluctuating velocities) are the controlling factors that determine their distribution. The direction of the injection is axial, and thus, the mass flow rate of the big droplets has a maximum near the axis and decreases rapidly with radial distance (Figure 15a). The profiles are progressively flattened downstream (Figure 15a) due to the interaction with the gas phase. In general, the dispersion of the big droplets increases with increasing swirl (Figure 15e) or decreasing droplet loading (Figure 15c) or, in other words, with increasing effective swirl number of the two-phase flow.

Small droplets. The dispersion of the small droplets follows three main steps: First, near the outlet of the burner, small droplets exhibit a concentration profile similar to that of the big droplets, namely a high concentration near the axis and lower concentration away from it ($x = 2D$, Figure 15b). Second, the droplets exchange momentum with the gas phase and so obtain a circumferential velocity, which pulls them away from the axis and near the jet edge, where a concentration maximum is formed ($x = 3.5D$, Figure 15b). Finally, the interaction of droplets with the gas-phase turbulence becomes the dominant factor, which further controls the dispersion ($x = 5D$, Figure 15b). The above process has been observed for all droplet loadings and swirl numbers. However, the more the effective swirl number of the two phases is augmented the more this process is shifted toward the injection slot point (Figures 15b, d, and f).

Total mass flow rate. Because of the different behavior of small and big droplets as they interact with the gas phase, the total mass flow rate per unit area exhibits two maxima; the first, near the axis, which is due to the presence of the big

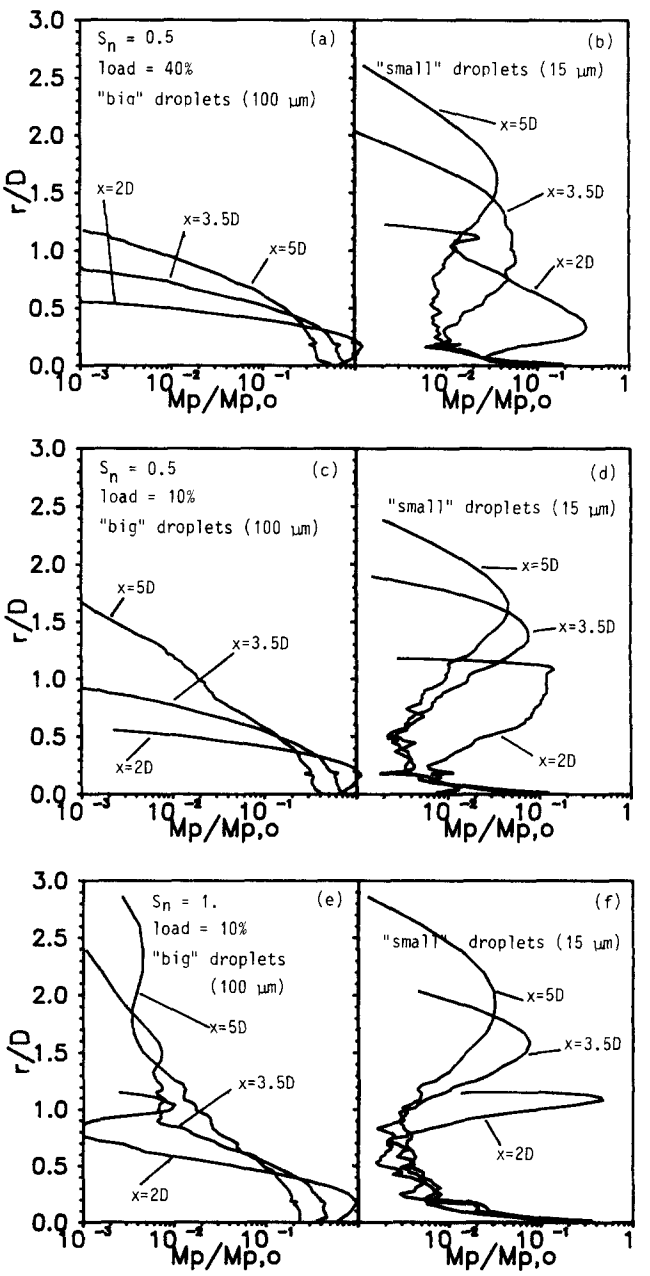

Figure 15 Profiles of droplet mass flow rate (Mp) per unit area at various axial positions: (a and b) $S_n = 0.5$, load = 0.4; (c and d) $S_n = 0.5$, load = 0.1; (e anf f) $S_n = 1.0$, load = 0.1

droplets and the second near the jet edge, due to the small droplets. Again, the higher the effective swirl number of the two phases is, the quicker (closer to the injection point) this pattern takes place (Figure 15).

The distribution function of the total mass flow rate has been drawn in Figure 16 for various swirl numbers and droplet loadings at an axial position $x = 3.5D$. From this figure, it is observed that the dispersion width of the droplets is increased as the effective swirl number increases. Also, with increasing swirl, the center of gravity of the liquid phase is moved away from the jet axis (Figure 17).

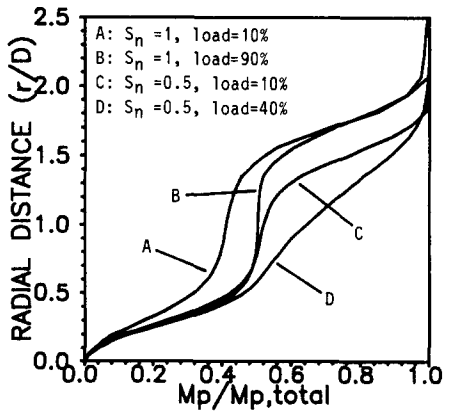

Figure 16 Distribution function of total droplet mass flow rate (Mp) at $x = 3.5D$

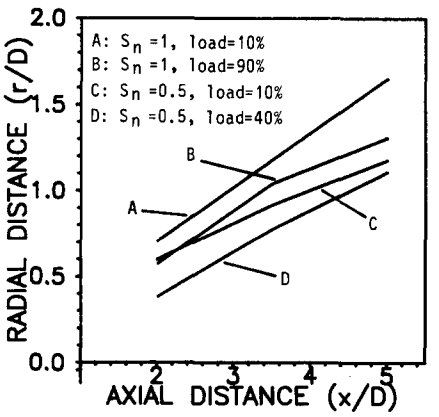

Figure 17 Center of gravity of the droplet phase at various axial stations

Droplet velocities. In Figure 18, there are plots of axial velocities of both droplet categories, together with the mean air velocitiy at various downstream positions for load = 10 percent and $S_n = 1$. From Figure 18, it is concluded that the big droplets, which penetrate into the IRZ, are affected a little by the reverse flow field. The maximum velocity of these droplets appears in a radial distance equal to the radial distance of their point of injection. However, there is a small percentage of the big droplets, obviously the smaller of this category, that follow the fluid (Figure 15e) and obtain velocities close to those of the air.

In contrast with the big droplets, the velocity of the small ones follows the velocity changes of the air throughout the computational domain, exhibiting a slight acceleration in the region near the boundaries of the IRZ, as mentioned previously.

Conclusions

The outcome of this study can be summarized as follows:

(1) The percentage of the recirculating mass is reduced as the droplet loading is increased or as their diameter is decreased. However, the position of the center of the IRZ is not altered.
(2) The length of the IRZ decreases with the increase of loading and its rate of decrease is higher for the bigger droplets.
(3) For high loadings and swirl, the initial recirculation zone can be subdivided into two recirculation subregions, due to the penetration of the discrete phase.
(4) The dispersion and the velocities of the big droplets studied are not affected significantly by the IRZ, but they depend on their inlet (injection) conditions.
(5) The small droplets are dispersed following the streamlines of the carrier phase, quickly attaining velocities close to those of the air.
(6) The total concentration profile of the discrete phase exhibits two maxima: the first near the axis, which is due to the presence of the big droplets and the second near the edges of the IRZ, due to the dispersion of the small droplets.
(7) The weight point of the liquid phase is moved away off the axis more quickly (at smaller axial distances) with increasing effective swirl number.

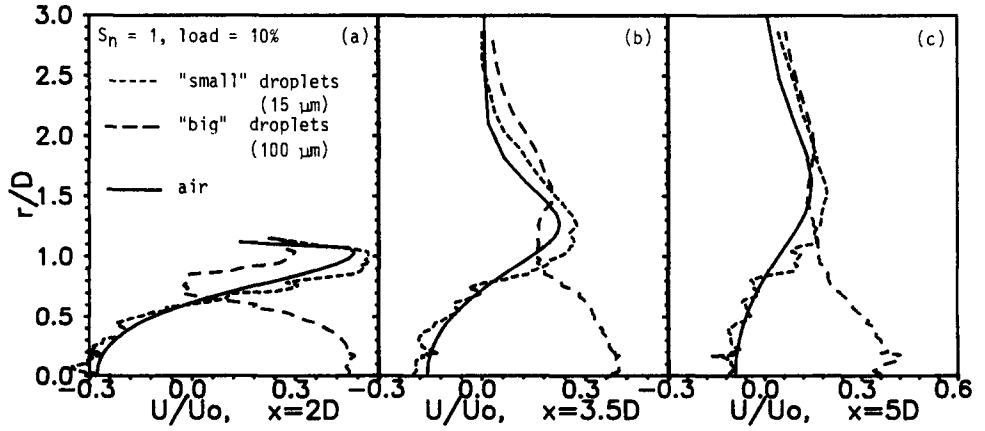

Figure 18 Axial velocity profiles at various axial locations for $S_n = 1$ and load = 0.1

The above study with its results are of engineering importance in the design of quarl burners and especially in pulverized coal combustion, although it is probable that certain of the aforementioned conclusions might change when combustion occurs.

Acknowledgments

The financial support of EEC/DGXII Solid Fuel Subprogram and the personal interest of Mr. Sens of EEC and Dr. A. K. Taylor and Professor J. H. Whitelaw of Imperial College is gratefully acknowledged.

References

1 Hardalupas, Y., Taylor, A. M. K. P. and Whitelaw, J. H. Velocity and particle-flux characteristics of turbulent particle-laden jets. *Proc. Royal Society London*, 1989, **A-426**, 31–78

2 Tsuji, Y., Morikawa, Y., Tanaka, T., Karimine, K. and Nishida, S. Measurement of an axisymmetric jet laden with coarse particles. *Int. J. Multiphase Flow*, 1988, **14**, 567–574

3 Laats, M. K. and Frishman, F. A. Scattering of an inert admixture of different grain size in a two-phase axisymmetric jet. *Heat Transfer, Soviet Research*, 1970, **2**, 7–12

4 Hayashi, K. and Branch, M. C. Concentration, velocity and particle measurements in gas-solid two-phase jets. *J. Energy*, 1980, **4**, 193–198

5 Hayashi, K. and Branch, M. C. Particle transport effects in gas-solid two-phase nozzle and jet flow. *Israel J. Technology*, 1983, **21**, 135–142

6 Dixon, T. F., Truelove, J. S. and Wall, T. F. Aerodynamic studies on swirled coaxial jets from nozzles with divergent quarls. *Trans. ASME J. Fluids Eng.*, 1983, **105**, 197–203

7 Liu, C. H., Nouri, J. M., Tse, D. G. N. and Whitelaw, J. H. Particle velocities in a swirling, confined flow. Imperial College, Mechanical Engineering Department, Internal Report FS/89/09, London, UK, 1989

8 Hardalupas, Y., Taylor, A. M. K. P. and Whitelaw, J. H. Velocity and size characteristics of liquid-fuelled flames stabilized by a swirl burner. *Proc. Royal Society London*, 1990, **A-428**, 129–155

9 Elghobashi, S. E. and Abou-Arab, T. W. A two-equation turbulence model for two-phase flows. *Physics of Fluids*, 1983, **26**, 931–938

10 Migdal, D. and Agosta, V. D. A source flow model for continuum gas-particle flows. *Trans. ASME J. Applied Mechanics*, 1967, **34**, 860–865

11 Durst, F., Milojevic, D. and Schonung, B. Eulerian and Lagrangian predictions of particulate two-phase flows: a numerical study. *Appl. Mathem. Modelling*, 1984, **8**, 101–112

12 Mostafa, A. H. and Mongia, H. C. Eulerian and Lagrangian predictions of turbulent evaporating sprays. *AIAA* Paper 86-0452, 24th Aerospace Sciences Meeting, 1986

13 Anagnostopoulos, J. and Bergeles, G. Numerical study of particle-laden jets: a Lagrangian approach. *Mathematical Modeling in Combustion and Related Topics* (C. M. Brauner and C. Shmidt-Laine, Eds.), Nato ASI Series E (Applied Sciences, No. 140), Martinus Nijhoff, Dordrecht, The Netherlands, 1988

14 Sargianos, N. P., Anagnostopoulos, J. and Bergeles, G. Turbulence modulation of particles, downstream of a two-phase, particle-laden, round jet. *International Symposium on Engineering Turbulence Modelling and Measurements*, Dubrovnik, Yugoslavia, 1990

15 Launder, B. E. and Spalding, D. B. *Mathematical Models of Turbulence*. Academic Press, London, 1972

16 Wallis, G. B. *One Dimensional and Two-Phase Flow*. McGraw-Hill, New York, 1969

17 Shuen, J. S., Solomon, A. S. P., Zhang, Q. F. and Faeth, G. M. A theoretical and experimental study of turbulent particle-laden jets. NASA CR-168293, 1983

18 Patankar, S. V. and Spalding, D. B. A calculation procedure for heat, mass and momentum transfer in three dimensional parabolic flows. *Int. J. Heat Mass Transfer*, 1972, **15**, 1787–1805

19 Sharma, M. D. and Crowe, C. T. A novel physico-computational model for quasi one-dimensional gas-particle flows. *Trans. ASME J. Fluids Eng.*, 1978, **100**, 343–349

20 Diakoumakos, H., Anagnostopoulos, J. and Bergeles, G. A theoretical study of solid-air, two-phase flow. *Mathematical Modeling in Combustion and Related Topics* (C. M. Brauner and C. Shmidt-Laine, Eds.), Nato ASI Series E (Applied Sciences, No. 140), Martinus Nijhoff, Dordrecht, The Netherlands, 1988

21 Sloan, D. G., Smith, P. J. and Smoot, L. D. Modeling of swirl in turbulent flow systems. *Prog. Energy Combustion Sci.*, 1986, **12**, 163–250

22 Leschziner, M. A. and Rodi, W. Computation of strongly swirling axisymmetric free jets. *AIAA J.*, 1984, **22**, 1742–1747